Promoting the use of Fe-rich slag in construction: Development of a hybrid binder for 3D printing

Cement and Concrete Composites 138 (2023) 104959

Contents lists available at ScienceDirect

Cement and Concrete Composites

journal homepage: www.elsevier.com/locate/cemconcomp

Promoting the use of Fe-rich slag in construction: Development of a hybrid binder for 3D printing

Glenn Beersaerts [a,*], Tobias Hertel [a], Sandra Lucas [b], Yiannis Pontikes [a]

[a] KU Leuven, Department Materials Engineering, Kasteelpark Arenberg 44, 3000, Leuven, Belgium
[b] University of Technology Eindhoven, Department Built Environment, Het Kranenveld 8, 5600, Eindhoven, Netherlands

ARTICLE INFO

Keywords:
3D printing
Non-ferrous metallurgy slag
Alkali-activated materials
Hybrid mortars
Rheology
Alternative binders

ABSTRACT

The construction sector is responsible for significant CO_2 emissions, especially due to the production of ordinary Portland cement (OPC). One option to decrease CO_2 emissions is to print mortar made from an alternative binder. A precursor was used consisting of mainly non-ferrous metallurgy Fe-rich slag and a minor amount of OPC (<16 wt%), which forms upon alkali-activation a hybrid binder. A 3D-printable hybrid mortar was developed in a step-by-step performance-based approach, with a focus on the fulfilment of criteria relevant for 3D printing: shear-thinning, high yield stress, and stiffness development. The criteria to be met were determined using a commercially available 3D-printable OPC-mortar. Several raw materials were introduced to develop a hybrid mortar with a particle packing that positively influenced the pumpability and buildability. The effect of the precursors and superplasticizer on reactivity was investigated. The final mortar reached the printing criteria, offering a suitable alternative to 3D-printable OPC-mortars.

1. Introduction

The digitalisation of processes in the construction sector is still running behind compared to other manufacturing sectors [1–3]. Implementing 3D printing can be a paradigm shift in construction with respect to digitalisation and has several advantages compared to the current construction process. 3D printing has the potential to be more economic and sustainable, as the construction process is faster, the customization is increased, less waste is generated and the formwork becomes superfluous [4,5]. The aforementioned advantages are one aspect when considering 3D printing, but the material to print with is another important aspect to address. If the material developed for printing is less sustainable compared to the material used nowadays in construction, it is less feasible to implement 3D printing in construction. Literature reports that most 3D-printed structures are printed with a cement-based mortar. These mortars consist of 55–70 wt% ordinary Portland cement (OPC) in the binder, the latter is thus considered as the main precursor [6]. Accelerators, such as calcium sulphoaluminate cement (CSA) can also be used in OPC mixtures to reach fast setting times (improving buildability) and high early strength. Due to the former, CSA is often introduced to the mixture at the print head right before extrusion. It is reported that up to 7% CSA can be added to the mixture, although its proportion needs to be properly chosen as the CSA hydration can result in the formation of expansive phases and voids [7–9]. Compared to conventional high-performance mortar, 3D-printable mortar is reported to contain 20% more OPC, as the binder to aggregate ratio is higher to obtain a pumpable and extrudable mixture with an accelerated early strength development [6,10]. Consequently, the environmental impact of the 3D-printable mortar is significant, as the production of 1 ton OPC is responsible for about 0.8 ton of CO_2 [11,12]. The CO_2 impact per m^3 of 3D-printable mortar is thus higher compared to a high-performance mortar [6]. This might be compensated to some extent through volume reduction of the structure as a simplified structure with optimised geometry can be printed (less over-engineering) without compromising performances [13]. Several supplementary cementitious materials (SCMs), such as fly ash (FA),

Abbreviations: NFMS, Non-ferrous metallurgy slag; OPC, Ordinary Portland cement; GGBFS, Ground granulated blast furnace slag; SF, Silica fume; FA, Fly ash class F; FL, Fine limestone powder; CS, Coarse quartz sand; SP, Superplasticizer; PCE, Polycarboxylate ether; MF, Microfibers; CSA, Calcium sulphoaluminate cement; L/S, Liquid over all solids mass ratio; L/B, Liquid over binder mass ratio; S/B, Sand over binder mass ratio; E-mod, Dynamic E-modulus; SEM, Secondary electron microscope; SCM, Supplementary cementitious materials; IP, Inorganic polymer; AAM, Alkali activated material.

* Corresponding author.
E-mail addresses: glenn.beersaerts@kuleuven.be (G. Beersaerts), tobias.hertel@kuleuven.be (T. Hertel), s.s.d.o.lucas@tue.nl (S. Lucas), yiannis.pontikes@kuleuven.be (Y. Pontikes).

https://doi.org/10.1016/j.cemconcomp.2023.104959
Received 3 August 2022; Received in revised form 16 January 2023; Accepted 26 January 2023
Available online 7 February 2023

silica fume (SF) and fine limestone (FL), are introduced in 3D-printable mortars with proportions reported around 40% of the binder to decrease the OPC content. A further replacement of the OPC by SCMs is limited as it would compromise the print quality and late age properties [6]. 3D printable blended cement mortars were developed consisting up to 60% of calcined clays and fine limestone in the binder [14,15]. A higher content of calcined clays was not recommended as it would increase the porosity and decrease the strength of the printed material [15].

The environmental footprint of 3D-printable mortars can be further reduced when using alkali-activated materials (AAMs), as in these materials OPC is not used. Limited research is conducted on 3D printing of AAMs, with most of it performed by Biranchi Panda, who studied alkali-activated mortar blends of FA and ground granulated blast furnace slag (GGBFS) [16–19]. The binder fraction of these mortars comprises FA class F (75–100 wt%), GGBFS (5–8 wt%) and SF (10–16 wt%), activated with a potassium or sodium-silicate solution [16–19]. Other researchers developed AAMs for 3D printing with a small scale ($49 \times 40 \times 30$ cm^3) extrusion printer in which the GGBFS content is higher in the binder (15–70 wt%) compared to the aforementioned binder formulation [20,21]. The availability of FA, which is the main binder component in aforementioned mixtures, is limited in comparison to OPC and is expected to decrease in future as other energy sources become more attractive than coal combustion [22,23]. Therefore, other potential precursors should be investigated, such as Fe-rich slags from the non-ferrous metallurgical industry, which are currently landfilled or used in low-value applications. These Fe-rich slags, of which the chemical composition differs significantly from GGBFS with respect to the Fe and Ca content, can form after alkali-activation a binder called inorganic polymer (IP) which is a subset of AAMs [24,25]. An IP can be a suitable alternative binder to OPC-based binders, in particular with respect to its mechanical performance [26]. Using Fe-rich slag instead of OPC can significantly reduce the environmental impact as shown in the work of Peys et al. [27]; however, IPs require an alkali solution with a high KOH/NaOH molarity, which is costly and its production process is associated with a significant environmental footprint [27,28]. Further, these alkali solutions reduce the effectiveness of organic-based admixtures, such as superplasticizers (SPs), due to the change in adsorption behaviour or the SPs break down as they are not alkali-resistant [29]. This limits the functionality of IP mixtures, in particular when these mixtures are engineered for high-performance applications, such as 3D printing.

To overcome the aforementioned challenges of AAMs, a hybrid system is suggested. A hybrid system is kind of a compromising technology between OPC and AAM systems and more functional than AAMs [24]. The precursors of hybrid binders are mainly SCMs or industrial by-products – mostly GGBFS, metakaolin and FA – and a minor amount (up to 30 wt% in the binder) of OPC [30,31]. The precursors (apart from OPC) are not hydrated and therefore an alkali-hydroxide or alkali-silicate solution [32] is used to enable dissolution of the main precursor and its participation in the binder formation. When an aluminosilicate (FA or metakaolin) and OPC blend is activated with a NaOH solution, a complex system of different binders is formed. The OPC hydrates to form a C–S–H binder, while the dissolution of the aluminosilicates results in the formation of a N-A-S-H binder. These binders coexist and interact with each other to form a C-A-S-H binder at a later age [33,34].

Concerning the use of Fe-rich slags in hybrid binders, limited research is conducted to demonstrate that Fe-rich slags actively participate in the binder formation and do not simply take on the role of filler material. Based on the results in the work of Arnout et al. [35], a hybrid binder formulation of 70 wt% Fe-rich slag from the non-ferrous metallurgical industry, 10 wt% OPC, 8 wt% limestone, 0.3 wt% bassanite, 0.8 wt% SP and a 1.2 M NaOH is suggested. In this hybrid formulation, SPs, engineered for OPC-based materials, are effective. The effect of the SP is increased when the hydration product ettringite is formed around the particles [36]. Ettringite can be formed when a sulphate source, such as bassanite, is added [37]. The plasticizing effect is one of the biggest advantages of hybrids over AAMs, as the SP proportion can easily adjust the rheological behaviour of the fresh hybrid mixture towards the desired process/application. These findings demonstrated that a binder can be formed from Fe-rich slag [38]. An alternative precursor was employed in the work of Hertel [39] who investigated the possibility of producing hybrid binders from an Fe-rich slag produced from the thermal modification of bauxite residue (and 8 wt% OPC), activated solely with the alkalinity of the bauxite residue slurry. Results showed that not only the OPC but also the modified bauxite residue slag contributed to the binder formation. The hybrid formulations could be altered, depending on the slag chemistry, to obtain proper reactivity and strength development. The identification of the binder was reported to be challenging in these complex systems [39].

Limited literature was found on incorporating Fe-rich slags in 3D printable materials. One reference investigated the use of Cu-slag as a fine aggregate in a cementitious 3D printable mortar [40]. Another reference reported the possibility to use an iron(calcium)silicate-rich slag as a precursor in hybrid mortar for 3D printing [41]. In the latter, the reactivity, strength and shrinkage of different hybrid mortars were investigated and were compared with a OPC-based 3D printable mortar. Based on this research, hybrids can be an interesting alternative to OPC-based 3D-printable mortars as similar late-age properties were reached, although a 3D-printable hybrid mortar was not developed yet. To obtain a 3D-printable mixture, the following rheological aspects need to be taken into account: open time, pumpability, extrudability and buildability. The open time is considered as the time period in which the material can be printed, which is related to the hardening or initial setting time [20]. The initial setting time depends on the reactivity of the mixture and its structural development in time. Most of the reported alkali-activated mixtures can only be printed for a short time ($\pm$20 min) due to their fast reactivity [42,43]. Short open times can result in poor layer bonding and therefore a delayed setting time should be envisaged. The SP can influence, whether desired or not, the open time as it can delay the reactivity [44,45].

Next to the open time, the pumpability is another important aspect and is related to the amount of force or energy applied to the material defined by the movement of the pump and by the travel distance from the pump to the extruder. The force applied to the material can result in stress build-up in the pump, which needs to be as low as possible to avoid a blockage [46]. To obtain a pumpable mixture, the shear stress and viscosity must be low at high rotational speed [47], which can be obtained by shear thinning of the material. Researchers measured the fresh properties of 3D-printable OPC mortars and identified that the viscosity must be situated between 39 and 21 Pa s and the yield stress between 0.6 and 0.27 kPa to obtain a pumpable and extrudable mixture [10,48].

During the printing process, one layer is printed on top of the existing one, without the presence of formwork to support the layers. This successive layer build-up results in an increase of mass or force exerted on the bottom layers. The bottom layers need to be able to support the top layers without significant deformation. To avoid significant deformation or collapse of the structure, defined as buildability, the printed layer needs to recover instantly from its shear-thinning behaviour in the pump and must obtain high yield stress. The fresh mixture needs to form an initial structure once extruded, which consists of certain strength preferably. This early strength can be achieved by introducing fibres, nanoparticles or accelerators [49,50]. Paul et al. [17] identified for OPC and geopolymer-based 3D-printable mortars the slump value, which must be situated between 1 and 3 mm or 2 and 6% of the total slump height to reach a certain buildability. The specific stress and viscosity values that need to be achieved at different shear rates and the early age strength evolution depend on the type of pump, printer and extruder and the scale of the structure to be printed [47].

As far as the authors know, no research is reported yet on the development of a 3D-printable iron(calcium)silicate-rich slag based hybrid mortar. The work herein aspires to bridge the gap in the

Table 1
The bulk chemistry of the precursors.

Element (wt%)	NFMS	FA	OPC
FeO_x total	35–46	7	3
SiO_2	20–31	55	20
CaO	11–21	4	64
Al_2O_3	2–7	23	5
Na_2O	0.5–2.5	1	0.2
MgO	0.5–2.5	2	1.5
SO_3	0.2–1	/	3.4
Other	2–7	2–8	3.2

Table 2
The amorphous and crystalline phases (wt%) of the precursors.

Phases (wt%)	NFMS	FA	OPC
Amorphous	70–85	90	–
Spinel	10–20	–	–
Wüstite	3–9	–	–
Quartz	0.1–1	10	–
C_3S	–	–	62
C_2S	–	–	10
C_3A	–	–	8
C_4AF	–	–	8
$C\hat{S}\cdot 2H$	–	–	5
$C\hat{C}$	–	–	3

literature by developing a new type of binder for printing. The development of a printable hybrid mortar from non-ferrous metallurgy slag (NFMS) can increase the valorisation potential for this type of slag. The print criteria (pumpability, open time, extrudability and buildability) are determined by a 3D-printable OPC-based mortar, called benchmark. From the proposed self-levelling hybrid formulation shown in Ref. [35], a 3D-printable hybrid mortar is developed in this research. This research tries to meet the print criteria by introducing SCMs, optimising the particle packing, varying the amount of SP and introducing microfibers. The contribution of each raw material to the reactivity and the open time is identified by assessing the heat flow development and the correlation of the latter with the dynamic E-modulus development. The pumpability and the structural recovery are investigated by rheological experiments. The buildability of the fresh mortar is identified and improved by measuring the early-age dynamic E-modulus development, the slump height and the maximum compression force. The microstructure is investigated using scanning electron microscopy. By mapping the chemical composition of the binder the contribution of the NFMS to the binder formation and the possible formation of different binder types can be identified.

2. Raw materials

The following precursors were used in the hybrid formulation: CEMI 52.5 R (OPC) from CRH, NFMS from Umicore and fly ash class F (FA) from Baumineral. The ultrafine materials comprise fine limestone powder (FL) from Euroment (Betofill) and silica fume (SF) from Elkem (Microsilica 920). Microscopic fibres (MF) were also introduced in the mixture as needle-shaped magnesium aluminosilicate clay minerals (Acti-gel 208, 5–100 μm length) provided by Faber&VanderEndere. Quartz sand (CS) was used as aggregate and sieved under 1.6 mm. The chemical bulk composition of NFMS was determined by X-ray fluorescence (XRF, spectrometer PW 2400, Philips) and the chemical composition of FA and OPC were received from the suppliers; all three compositions are shown in Table 1. The chemical and mineralogical composition of the NFMS is shown as a range, as requested by the slag supplier. The FeO_x total in Table 1 comprises FeO, Fe_2O_3 and Fe.

The mineralogical composition of NFMS was analysed by X-ray diffraction (XRD) in a range of 5°–70° 2 Theta using a D2 Phaser (Bruker) operating at a voltage of 30 kV and a current of 10 mA. The

Table 3
The specific density and the D_{10}, D_{50} and D_{90} (μm) of each raw material.

Raw material	D_{10}	D_{50}	D_{90}	Specific density (g/cm^3)
NFMS	1.6	8.4	47.1	3.4
FA	1.4	12.9	54.2	2.3
OPC	0.9	5.8	16.8	3.1
FL	1.0	5.7	16.8	2.7
SF	0.1	0.2	0.5	2.2
CS	348.5	544.2	790.2	2.5

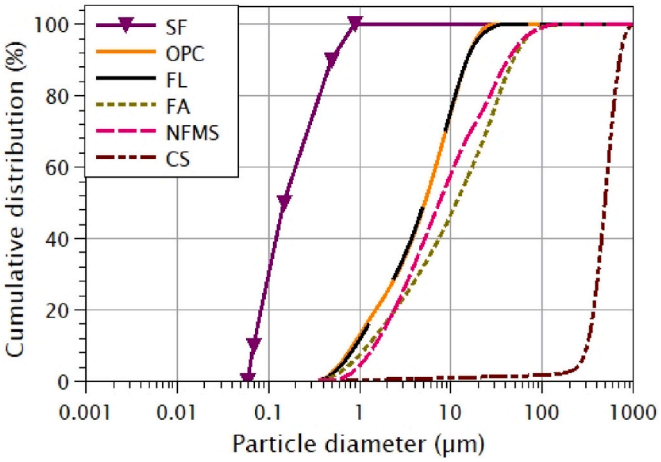

Fig. 1. The PSD of the raw materials.

crystalline phases and amorphous content were quantified on a blend composed of NFMS and 10 wt% of the internal standard ZnO, after milling in a McCrone micronizing mill using hexane (>99% pure) as milling media and ZrO grinding elements [51]. The amorphous and crystalline phases obtained by XRD-analysis, are shown in Table 2. In this research, the chemical formula is written according to the cement nomenclature, i.e. C= CaO, S = SiO_2, A = Al_2O_3, F = Fe_2O_3, K = K_2O, Na = Na_2O, $\hat{S}$ = SO_3, H = H_2O, $\hat{C}$ = CO_3.

The specific density of the raw materials was measured by a pycnometer according to ASTM-B417-64 and is shown in Table 3. The specific density is the highest for NFMS, followed by OPC, FL, FA, CS and SF. The particle size distribution (PSD) of each raw material was determined by laser diffraction in ethanol (Beckman Coulter LS 13 320). Table 3 indicates that SF has the smallest D_{50} (0.15 μm), followed by FL (5.7 μm), OPC (5.8 μm), NFMS (8.4 μm), FA (12.9 μm) and CS (544.2 μm). The cumulative PSD of each raw material is plotted in Fig. 1. SF presents the ultrafine fraction of the raw materials, followed by OPC and FL, the last two having a similar PSD. The PSD of NFMS and FA are similar, and both have a slightly wider PSD (larger fraction of coarser particles) compared to OPC. The CS represents the coarsest material and a narrow PSD.

3. Methodology

3.1. Benchmark material

A commercially available OPC-based 3D-printable mortar was used as a benchmark to determine the print criteria that need to be reached. The exact composition of the benchmark is unknown, and the supplier cannot be disclosed. However, the mortar probably consists of an optimised particle packing, with varying quantities of OPC (CEM I, 52.5 R), quartz sand <1 mm, FL, rheology admixtures (organic-based, such as polycarboxylate ether (PCE) SPs) and polypropylene fibres. The dry solids were hydrated with a water to solid mass ratio of 0.16.

Table 4
The investigated hybrid mix formulations. In bold the parameter that is investigated in each particular mixture.

Raw material (wt% in binder)	Basic formulations (B)				3D printing developing formulations (D)					
	B1	B2SP	B3BA	B4SP	D1FL	D2FA	D3SF	D4CS	D5SP	D6MF
OPC	19.7	19.6	19.6	19.6	13.8	13.8	13.8	13.8	13.8	13.8
NFMS	80.3	79.6	79.3	79.6	77.7	62.9	55.6	55.5	56.0	55.9
FL	/	/	/	/	**7.4**	7.4	7.4	7.4	7.4	7.4
FA	/	/	/	/	/	**14.7**	14.7	14.7	14.7	14.7
SF	/	/	/	/	/	/	**7.4**	7.4	7.4	7.4
SP + BA	/	**0.8**	**1.1**	**0.8**	1.1	1.1	1.1	1.1	**0.6**	0.6
MF	/	/	/	/	/	/	/	/	/	**0.2**
L/S	0.17	0.09	0.09	0.09	0.09	0.09	0.09	0.08	0.09	0.09
L/B	**0.4**	0.2	0.2	0.2	0.2	0.2	0.2	0.2	0.2	0.2
S/B	1.0	1.0	1.0	1.0	1.0	1.0	1.0	**1.4**	1.0	1.0
Bulk density (g/cm^3)	2.18	2.44	2.44	2.44	2.43	2.39	2.36	2.38	2.36	2.36

3.2. Particle packing

A self-levelling hybrid mortar, derived from Ref. [35], was used as the reference mortar or starting mixture (formulation D1FL in Table 4) and was engineered towards a 3D-printable hybrid mortar. When combining the correct proportion of each raw material an ideal packing can be achieved, which can increase the flow of the mixture [52]. An ideal particle packing selects a specific amount of particles with a certain size to ensure that all the voids between the larger particles are filled with smaller particles, a process that can be continued until the smallest particle size is reached (minimum particle size). In this research, a continuous particle packing curve was targeted, calculated by the modified Andreassen model, with a minimum particle size of 0.05 μm and a maximum particle size of 1000 μm. A q-value is used in the modified Andreassen model to modify the packing curve gradient, as the proportion of coarse and fine materials can differ depending on the intended application. A q-value of 0.27 is typically used for high-performance concrete, while self-levelling concrete has a $q < 0.22$ [53]. The particle packing was improved by using a commercial particle packing software, called EMMA (from Elkem). The proportion of NFMS, OPC, FL, CS in D1FL was changed, and FA (D2FA) and SF (D3SF) were introduced into the mixture to improve the particle packing. A sand over binder ratio of 1 was suggested by the particle packing software and the sand/binder ratio was similar for all hybrid mixtures, apart from D4CS. In the latter formulation, the CS was increased to investigate its contribution to the rheology. When FA and SF were introduced in a formulation, a proportion of respectively 14.7 and 7.4 wt% had to be used to obtain a particle packing similar to the desired packing given by the software. Further, the particle packing software calculated the bulk density of each formulation (Table 4).

3.2.1. Raw materials and sample preparation

A 1 M KOH solution was used as an activator and was produced by dissolving KOH pellets (98% purity, Sigma Aldrich) in tap water at least 24 h prior to mixing. Two additives were used to create the plasticizing effect, a Melflux 4930 F PCE SP from BASF and a 99% pure bassanite (BA) from Sigma Aldrich. Before the mortar preparation, the SP and BA were introduced into the alkali solution during mixing within 30 s at low speed (130 rpm) with a 5 L Hobart. Afterwards, OPC, NFMS, FA, SF and FL were gradually added during mixing within 1 min and mixed for another minute at low speed. When fibres were used, the fibres were introduced during the paste preparation. Finally, the sand was added during mixing within 1 min and the blend was mixed for another minute at high speed (220 rpm). The prepared mixture was cast in the mould for the appropriate test and the aforementioned mixing procedure (total mixing time 4 min) was applied for all experiments and all formulations mentioned in Table 4, including the benchmark. The curing conditions for each sample depended on the test the sample underwent and therefore the curing is explained in the methodology section of each test.

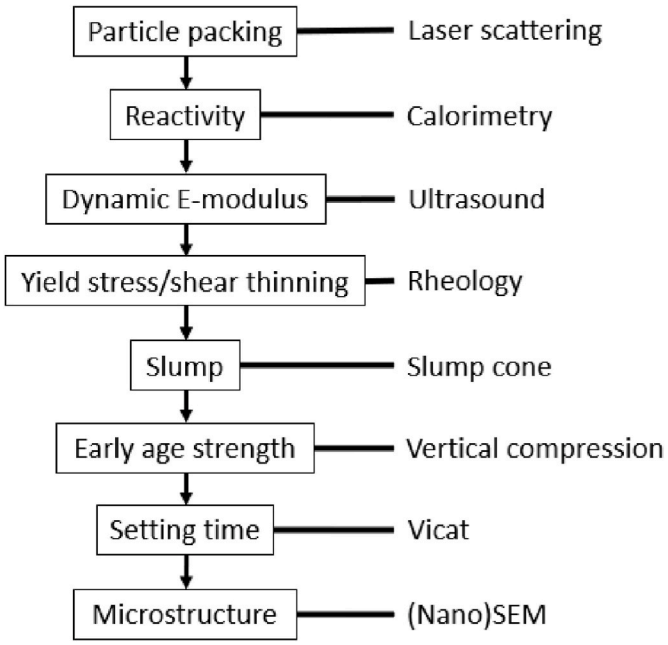

Fig. 2. The stepwise performance-based mix design development approach.

3.2.2. Performance-based mix design development

The first series of mixtures are hybrid (B) formulations B1, B2SP, B3BA and B4SP, which are mixtures solely made to determine the contribution of OPC, NFMS, BA and SP to the reactivity. These mixtures are based on the work done in Ref. [35] and do not contain any other raw material apart from the alkaline solution, the aforementioned components and CS (Table 4). The second series of mixtures comprised the formulations developed toward 3D printing (D), starting with the initial self-levelling hybrid mortar (D1FL), which was modified stepwise to investigate the effect of each new raw material added to the mixture or by changing the proportion of a certain raw material. First, the effect of FA (obtaining formulation D2FA) was investigated, next SF (D3SF) and in mixture D4CS the proportion of CS was modified. In formulation D5SP the amount of SP was decreased. The final mixture (D6MF) studied the effect of MF. The investigated parameter for each mixture is indicated in bold in Table 4. The OPC content in the B-formulations was slightly higher compared to the D-series to ensure that the effect of SP and BA on the reactivity could be properly investigated. Formulation D1FL and the proportions of SP and BA in all mix designs were based on the mixture developed in Ref. [35]. 0.3 wt% of BA was used and remained constant for all investigated mixtures. 0.8 and 0.3 wt% of SP was used depending on the formulation as the amount of SP can affect the performance significantly. A liquid to binder (L/B) ratio of 0.2 was used for all hybrid formulations apart from B1. The L/B ratio in B1 had

Table 5
This table indicates which mix design underwent which test(s).

Methods	Hybrid formulation										Benchmark
	Basic: B-				Developed for 3D-printing: D-						
	1	2SP	3BA	4SP	1FL	2FA	3SF	4CS	5SP	6 MF	
Calorimetry					✔ (without CS)						/
Ultrasound	/	✔	✔	/	✔	✔	✔	/	✔	✔	✔
Rheometer	/					✔					✔
Slump			/			✔	/	✔	✔		✔
Vertical deformation				/					✔		✔
Vicat				/					✔		✔
SEM	✔ (without CS)					✔					/

to be increased to 0.4, to ensure a castable mixture, as a SP was not used in this formulation. The alkalinity of the activator was determined from preliminary tests which indicated that an alkalinity higher than 1 M KOH drastically decreased the SP effectiveness. The proportion of CS, FA and SF for each formulation were suggested by the particle packing software as explained in chapter 3.2. The sand/binder ratio was similar for all hybrid mixtures, apart from D4CS. In the latter, the CS was increased to investigate its contribution to the rheology. The amount of SP used in D5SP was determined by preliminary scanning, in which the SP content was gradually decreased until the rheological criteria were reached. A small amount of MF was introduced in D6MF, of which the amount was determined from preliminary tests. Only a certain amount of MF could be used to avoid that the measurement limit of the rheometer was reached.

This research followed a stepwise performance-based mixture development approach (Fig. 2), in which first various mixtures were investigated and when the research evolved, the investigation narrowed down to the best-developed mixture (D6MF in that case). For each experiment, the OPC benchmark was measured to identify the criteria or desired behaviour that needs to be obtained. In this way, a mixture was developed that performed the best according to the investigated range of parameters. It is nonetheless acknowledged that this is not the overall optimal mixture, but resembling as good as possible the properties of the benchmark. The optimal 3D printing mixture can be developed in future research through a design of experiments approach or by applying machine learning models. With the stepwise performance-based mixture development approach, not all mix designs were investigated with all methods used in this research, as shown in Table 5. For instance, the B-formulations were mainly used to investigate the heat flow, the dynamic E-modulus and the microstructure. The more suitable the mixture became for 3D printing, the more experiments it underwent. For instance, the final mixture D6MF was – according to reactivity, rheology, and slump tests –the most optimised mixture for 3D printing. Therefore, it underwent additional tests, such as setting time and vertical deformation tests to ensure it reached all print criteria.

Several samples are duplicated in some tests to obtain an idea of the variability/repeatability of each test. Basically, rheology showed very low variability, the obtained curves were partially overlapping. Calorimetry and ultrasound data for duplicated samples showed low variability, apart from the ones that are discussed in the results. Error bars are not shown in the results as the figures would become unreadable. Although the variability between the replicates is relatively low, a more extended dataset of each sample could result in a lower P-value. The latter indicates whether the samples are statistically different or not. Nevertheless, the actual obtained results should be sufficient for this study to reach the main goal, which is the development of a mix design with properties similar to the benchmark.

3.2.3. Isothermal calorimetry

The reaction kinetics of each paste formulation (Table 5, CS was left out) were investigated using an isothermal calorimeter at 20 °C (TAM Air, TA Instruments). Each blend was externally mixed manually for 4 min and introduced in the calorimeter 4 min after mixing. Three duplicates were made to determine the repeatability of the mixtures and showed that the data did not vary more than 10% of the mean value and thus showed a similar heat flow curve.

3.2.4. Ultrasound tests

The dynamic E-modulus (E-mod) development was measured with an ultrasonic pulse device according to EN 12504-4 [54]. All formulations from Table 4 were tested, apart from B1, B4SP and D4CS as they are non-optimised mixtures. D4CS does not follow the desired particle packing and consists of more CS, which was merely interesting for rheology. The ultrasonic pulse measurement started from the moment the fresh material was cast in a cylindric silicone mould, which was around 4 min after mixing, and lasted up to 48 h. The ultrasonic probes operated at a frequency of 30 kHz. The device transmitted every 10 s a sonic pulse (P-wave) that travelled through the sample and was captured by the receiver. The travel distance of the pulse between the transmitter and receiver was 40 mm, which is the width of the sample. Depending on the stiffness of the material, the pulse required a certain travel time (time delay) to move through the sample. From the travel time, the velocity v of the compression wave and E-mod were calculated according to the Newton-Laplace equation (Eq. (1)), with k-factor 0.876 and density (ρ) 2.1 g/cm^3 for the benchmark and between 2.2 and 2.4 g/cm^3 for the hybrid mixtures (bulk densities given in Table 4). The variability was investigated by reproducing samples B3BA, D2FA, D5SP and D6MF. The duplicates showed a similar stiffness development. Certain variability for the duplicates D5SP and D6MF was noticed at early age (up to 20 h), while at late age (48 h) the values are similar. The individual E-mod curve for each sample is presented.

$$E_{dyn} = k\ v^2\ \rho \quad (1)$$

3.2.5. Rheometer

Once the reactivity and E-mod were assessed, the effect of the raw materials FA, SF and CS, and the amount of SP and MF on the rheological behaviour were investigated. The investigated mixtures comprised the benchmark and all hybrid developing formulations (D-series in Table 4). Samples D2FA, D3SF and D6MF were repeated and the duplicates are overlapping, indicating insignificant variability. The rheological behaviour was measured with an Anton Paar rheometer (MCR 52) that consisted of a building material cell with a two-bladed vane impeller to investigate the yield stress and shear-thinning behaviour of the mixtures. The first rheological measurement started 3 min after mixing in which a rotational speed of 12 rpm was applied to the mixture for 60 s, followed by a rotational speed of 0.3 rpm for another 60 s. Afterwards, a flow sweep test was performed, in which the rotational speed was increased from 0.01 to 100 rpm and afterwards decreased from 100 to 0.01 rpm with a logarithmic step size. At each rpm increase or decrease, the rotational speed remained constant for 15 s to obtain accurate stress and viscosity values.

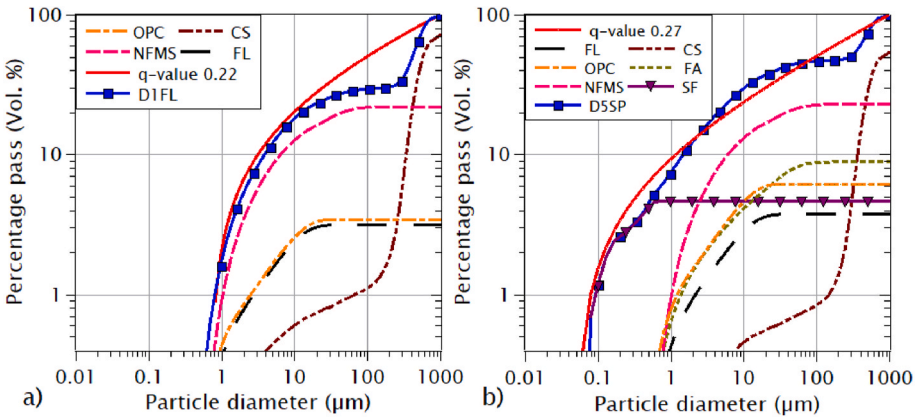

Fig. 3. Panel (a) the individual PSD of D1FL, the used raw materials (in proportion) and the modified Andreassen curve with a q-value of 0.22. Panel (b) the individual PSD of D5SP, the used raw materials (in proportion) and the modified Andreassen curve with a q-value of 0.27.

3.2.6. *Slump cone test*

The slump cone test was used to measure the consistency and yield of the benchmark, D3SF, D5SP and D6MF and was performed according to ASTM C143 [55]. The other formulations exhibited self-levelling characteristics and were thus not investigated. The cone has a height of 65 mm, an upper diameter of 40 mm and a lower diameter of 90 mm. The cone was filled with freshly mixed material and lifted 10 min after starting mixing. Afterwards, the height difference of the slump was measured and the slump type was identified. The test was not repeated and the individual values of each sample is given.

3.2.7. *Vertical deformation test*

A vertical deformation test, explained in detail in Ref. [56], was applied to the benchmark and the most promising hybrid mortar D6MF. The latter was chosen based on the rheology and ultrasound results. By compressing the sample, the maximum force that the material could withstand was identified, which can give insights into the buildability. The fresh material was cast in a cylindrical mould and tapped several times to remove entrapped air in the material. The cylindrical mould has a diameter of 70 mm and height of 140 mm, dimensions according to ASTM D2166 [57]. Further, each sample was placed in an Instron device with a 5 kN load head. The mould was carefully removed from the sample at a specific time (15, 30 and 90 min after mixing) right before testing and each sample was compressed at a 30 mm/min compression rate until a vertical displacement of 50 mm was reached. The force (N) was monitored to identify the peak force, which is the force at which the material failed. The test was repeated once for each sample and the average force with standard deviation is given.

3.2.8. *Vicat setting time*

The setting time was measured for the benchmark and the most promising mortar D6MF with the Vicatronic automatic Vicat recording

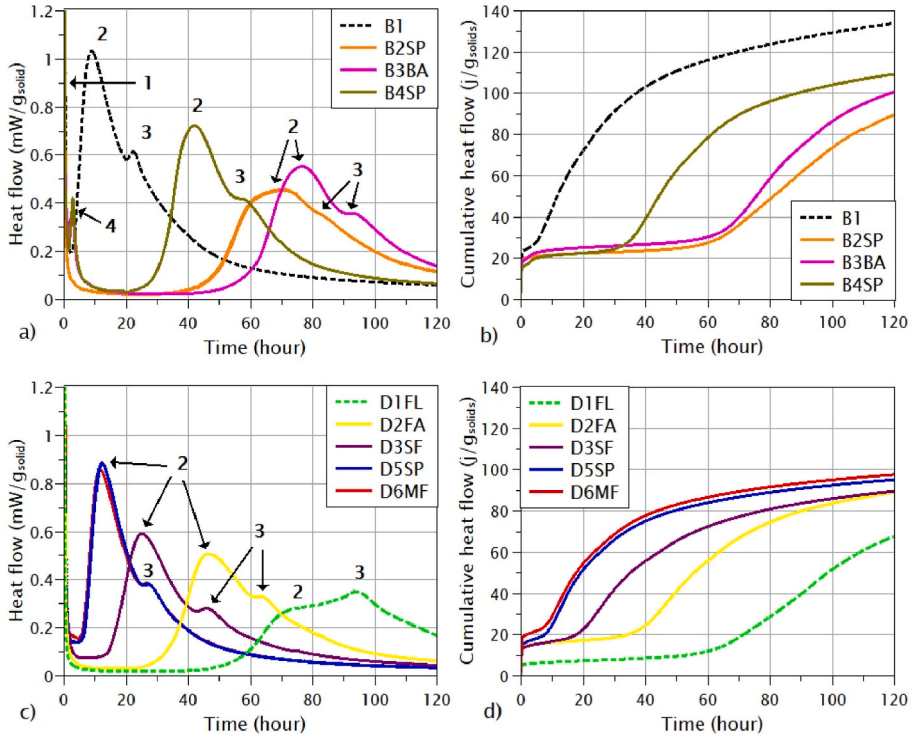

Fig. 4. (a) the individual heat flow evolution of B1, B2SP, B3BA and B4SP for 120 h and (b) individual cumulative heat flow for the same samples. Panel (c) the individual heat flow evolution of D1FL, D2FA, D3SF, D5SP, D6MF for 120 h and (d) the induvial 120 h cumulative heat flow for the same samples. The aforementioned samples are pastes, sand was not used for this test.

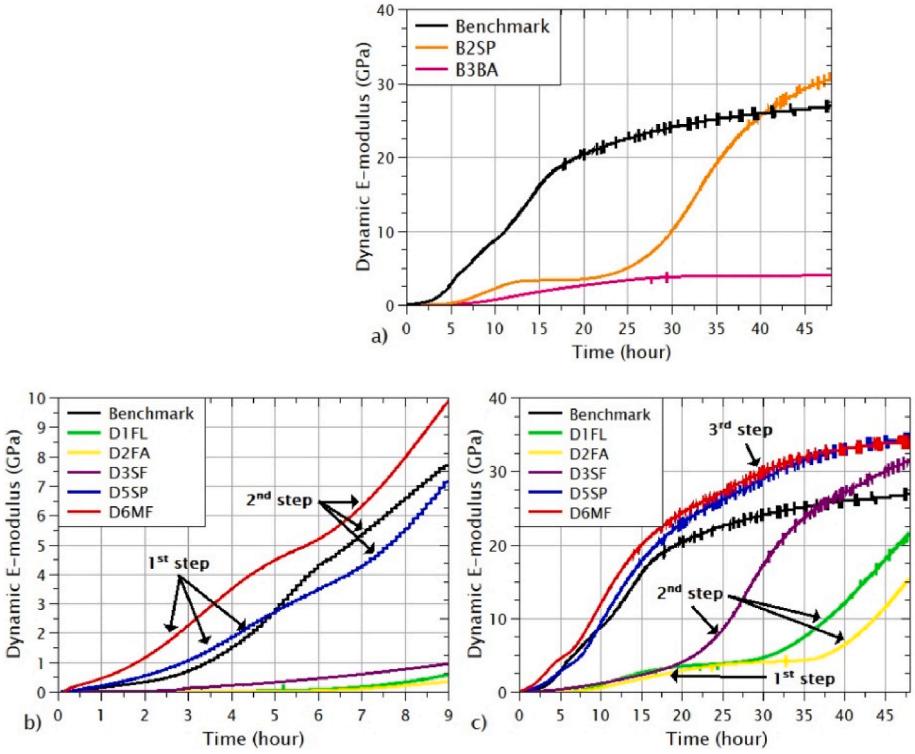

Fig. 5. (a) the individual E-mod development of the benchmark, B2SP and B3BA for 48 h long. Panel (b) the individual E-mod of the benchmark, D1FL, D2FA, D3SF, D4SP and D6MF for 9 h long and (c) for 48 h long.

apparatus according to EN 196-3 [58]. The mortar was cast in a circular sample holder and placed in the Vicat device. The Vicat measurement started 5 min after mixing. At certain pre-set moments the Vicat needle fell into the mortar with gravitational falling speed. 86 penetration depths were taken for the benchmark and D6MF in a time period of 8.2 and 5.7 h respectively. The initial and final setting time could be determined from the evolution in penetration depth results. The test was not repeated, consequently the individual result of each sample is given.

3.2.9. Scanning electron microscopy

Hybrid paste (without CS) cubes (2 × 2x2 cm^3) of each formulation (Table 5) were produced and cured for 28 days at 20 °C and 65% RH, from which fragments of cross-sections were embedded in epoxy resin, polished and coated with a 5 nm Pt layer. The microstructure was characterized with a Philips XL30 FEG scanning electron microscope (SEM) and a FEI Nova NanoSEM 450, both operating at 20 kV, at spot size 5 to obtain high-resolution backscattered electron images. Qualitative point analysis was performed with an energy dispersive X-ray detector to determine the elemental chemistry of certain phases by point analysis. Elemental mapping was carried out additionally.

3.3. Results and discussion

3.3.1. Particle packing

The PSD of D1FL partially corresponded with the modified Andreassen curve for self-levelling mixtures in which the q-value is 0.22 and the minimum particle size is 0.7 μm (Fig. 3). 3D-printable mixtures are situated in the high-performance window and therefore the q-value was increased to 0.27 and smaller particle sizes (0.05 μm) are desired [59]. This resulted in a modified Andreassen curve shown in Fig. 3B. A particle packing of the dry solids (D3SF) similar to the desired packing curve was obtained when replacing 14.7 wt% of NFMS by FA, 7.4 wt% of NFMS by SF and by lowering the sand over binder (S/B) mass ratio from 1.7 to 1.0. The decrease in sand resulted in a larger fraction of fine materials which is necessary to obtain high-performance mortars [60, 61]. SF accommodates the ultrafine fraction (Fig. 3B) of the particle packing curve. The particle packing curve D1FL in Fig. 3A shows that particles were absent from 52 to 250 μm, resulting in a 'gap' in the curve. This gap is in Fig. 3B partially covered by introducing FA as it has a wider PSD (D_{90} of 54.2 μm), although a gap between 90 and 200 μm remains visible. In future, the mixture can be optimised by covering this gap, for instance, with fine sand that consists of this particular PSD.

3.3.2. Calorimetry

The reactivity of the hybrid binders was assessed by monitoring the heat flow (Fig. 4) and showed for all investigated samples an initial peak at the start of the measurement. This peak can be allocated to the heat generated from the wetting of the particles, early dissolution of the precursors and the possible formation of initial hydration phases [62]. B1, the most simplified formulation which consists of only NFMS, OPC and activator, showed a 2nd peak around 10 h post mixing (peak 2 assigned in Fig. 4A), which is likely related to the OPC hydration and was higher compared to all other investigated mixtures as more activator was used [63]. A 3rd peak (peak 3 in Fig. 4A), situated 22 h post mixing, might be related to the NFMS dissolution and its contribution to the binder formation. In B2SP, SP was added to the formulation and the amount of water was decreased, resulting in a delayed hydration peak at 66 h and a shoulder at 80 h; the latter is likely related to the slag reaction (3rd peak). The delay in reactivity might be related to the SP which is adsorbed on the OPC particles and hydration phases [64–66]. In this way, further reaction of OPC could be delayed. Samples B3BA and B4SP showed the presence of an additional reaction peak (peak 4 in Fig. 4A) which is related to the introduction of BA. This reaction peak might be allocated to the formation of additional ettringite [67]. The latter is an important phase, as it prevents the mixture from false setting and provides a strong positive surface area on which the SP can adsorb [34]. Ettringite probably did not only cover OPC particles but also NFMS particles. In this way, the surface area on which the SP can adsorb might be further increased. B3BA generated more heat compared to B2SP (Fig. 4B) due to the additional reaction peak and the induction

(dormant) period is prolonged as the main hydration reaction is delayed [68]. This delay might be explained by the formation of ettringite and a geochemical barrier covering the OPC and probably NFMS particles [69]. The ettringite is stable and the reaction with the OPC is hindered as long as there is a sufficient supply of sulphates. When decreasing the SP amount (B4SP), the 2nd reaction peak and its shoulder is accelerated from 75 to 41 h and from 93 to 58 h, respectively, confirming once again that the amount of SP has a significant effect on the reactivity.

The heat flow evolution of D1FL, D2FA, D3SF, D5SP and D6MF (all are without CS) is given in Fig. 4C. D1FL showed the slowest reaction with the lowest amount of cumulated heat flow over time, followed by D2FA, in which the 2nd peak and the 3rd peak (peaks 2 and 3 assigned in Fig. 4C) can be better distinguished and took place at 47 and 64 h, respectively. The samples presented in Fig. 4C did not show an ettringite peak, unlike D3BA and D4SP (Fig. 4A), although BA is present in these mixtures. It might be possible that the ettringite peak merged with the initial peak due to the accelerated reactivity. The introduction of FA clearly accelerated the reactivity with 30 h (Fig. 4C). FA is already used in hybrid binders and its contribution of Si and Al-species to the binder formation is proven [32,70]. The reactivity is further accelerated when SF was added (D3SF). SF is, like FA, an SCM and can offer nucleation sites due to its small particle size (nano size) on which binder can precipitate [71]. Furthermore, SF likely dissolved partially once introduced to the alkaline environment as it is a reactive pozzolana [72]. This partial dissolution can bring more silicates into the solution and consequently reaching faster the saturation threshold to precipitate binder. The decrease in SP (D5SP) further accelerated the reactivity and slightly increased the cumulative heat flow (Fig. 4D). D6MF and D5SP have overlapping heat flow curves, indicating that MF probably did not react. The start of the acceleration period of the cement hydration (2nd peak) for D6MF and D5SP took place at 5 h and reached its maximum at 12 h. The NFMS contribution (3rd peak) took place around 27 h.

3.3.3. Dynamic E-modulus development

The E-mod development is an indication for the stiffness of the samples during the first 48 h and is presented in Fig. 5. B2SP showed a slight increase in E-mod at hour 8 (Fig. 5A), which might be related to the decrease in SP effectiveness. The SP might be consumed or might be broken down by the increased alkalinity due to the hydration reactions [73]. SPs are only temporarily effective and once the repulsion and steric hindrance effect is gone, the possibility of flocculation is increased due to the attractive interparticle forces. In this case, the material can build an internally connected structure which decrease the workability, without necessarily forming a binder. The E-mod accelerated after 25 h and is likely related to the formation of binder, as it coincided with the acceleration period of the cement hydration peak (shown in Fig. 4A). The latter probably increased the interparticle connectivity of the mortar. B3BA did not show any significant stiffness increase related to the formation of the binder during the first 48 h, as supported by heat flow evolution (Fig. 4A), indicating that the formation of ettringite and the steric hindrance from the SP prolonged the dormant period.

The introduction of FL (D1FL) accelerated the E-mod significantly (Fig. 5B) as the number of nucleation sites increased [74]. Two acceleration steps can be identified from the curve, one at 5 h (1st step in Fig. 5C), likely related to the decrease in SP effectiveness, and the other at 30 h (2nd step). The 2nd step, visualised in Fig. 4C, is probably related to the offset of cement hydration and binder precipitation [62]. The addition of FA did not accelerate the E-mod, which is not in line with the heat flow results. Based on the E-mod and heat flow results, it can be stated that FA contributes solely to the reactivity but not to the stiffness or connectivity of the mortar.

The introduction of SF (D3SF) did not affect the 1st step, while the 2nd step was accelerated, from 35 to 18 h; the latter coincides with the cement hydration peak and proves that SF accelerates the binder formation. SF can act as a contact bridge between two particles (precursors or FL) and increases the packing density (Fig. 3B) in the mixture [53].

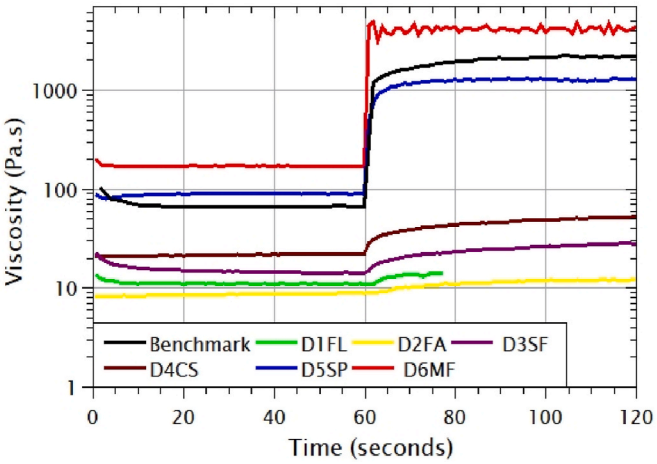

Fig. 6. A constant shear rate of 12 rpm for 60 s, followed by a constant shear rate of 0.6 rpm for the benchmark, D1FL, D2FA, D3SF, D4CS, D5SP and D6MF.

Both aforementioned factors can contribute considerably to the connectivity and might give rise to a gradual increase in E-mod from 2.5 h onwards. The E-mod at 48 h is twice as high when SF is introduced, 32 GPa versus 15 GPa without SF (D2FA), indicating that SF contributes to the stiffness of the mortar. The E-mod of D3SF at 48 h is higher compared to the benchmark, which is not the case at early age as the E-mod of the benchmark started to increase already after 15 min. However, such early-age E-mod increase is important for the buildability.

A decrease in the amount of SP (D5SP) results in an immediate E-mod increase at the start of the measurement (Fig. 5C). The first 7 h shows a constant rate in E-mod increase, probably related to the decrease in workability [75], as more flocs and colloids and less free water is present. Further, the cement and NFMS dissolution is not hindered as there is no excess in SP and the steric hindrance effect from the SP is decreased. After 7 h, the E-mod gradient of D5SP increased (2nd step in Fig. 5B), which is likely related to the precipitation of binder phases, as it coincides with the hydration reaction peak (Fig. 4C). The 2nd step finishes around 17 h, which coincides with the deceleration period of the cement hydration peak and thus marks the end of the main binder precipitation. The E-mod development of D5SP was similar to the benchmark up to 15 h and started deviating afterwards, in which the E-mod of D5SP continued to increase (3rd step in Fig. 5C), while the E-mod of the benchmark decelerated. The steady-state increase of D5SP is likely related to the NFMS contribution, as this event coincides with the 3rd reaction peak (shoulder in Fig. 4C). This indicates that the NFMS did not only react, but also contributed to the stiffness of the mortar. The E-mod of D3SF at 48 h is evolving towards the E-mod of D5SP, suggesting that the SP effect is worn off at late age. The introduction of MF resulted in a slight increase in average E-mod during the first 5 h of the measurement (Fig. 5B) and a much lower variability compared to the variability between the replicates of D5SP. The curves of D5SP and D6MF are closely together and their error bars (not shown here for sake of simplicity) partially overlap, therefore it can be stated that the curves of the 2 samples are statistically not different. The slight increase in average E-mod and decrease in standard deviation of D6MF during the first hours can be related to the interlocking effect of the fibres, which enhanced the connectivity and stiffness of the fresh material [76]. The E-mod of D6MF at 48 h is similar to D5SP, indicating that the MF did not affect late-age stiffness.

3.3.4. Rheology

The viscosity is shown in Fig. 6 and indicates that for D1FL and D2FA hardly any change in viscosity was observed when the rpm decreased from 12 to 0.6. The introduction of FA (D2FA) facilitated the flow

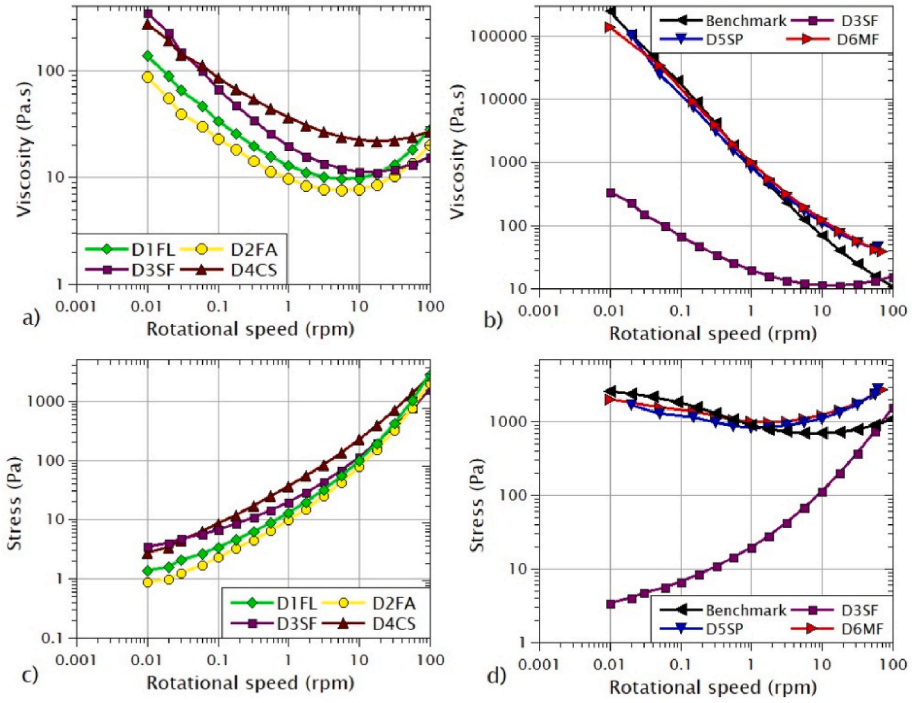

Fig. 7. The evolution in viscosity with rotational speed of D1FL, D2FA, D3SF and D4CS in (a) and of the benchmark, D3SF, D5SP and D6MF in (b). Panel (c) shows the evolution in stress with rotational speed of D1FL, D2FA, D3SF and D4CS and panel (d) shows the stress evolution of benchmark, D3SF, D5SP and D6MF.

behaviour even more, as for both shear rate regimes a slight decrease in viscosity (9.1 and 11.9 Pa s) is measured compared to D1FL. The introduction of SF slightly increased the viscosity in the 12 rpm regime to 14 Pa s compared to D2FA and showed a stronger recovery to a higher viscosity value (54 Pa s) in the 0.6 rpm regime. A higher sand to binder ratio (D4CS) shows an overall increase in viscosity without affecting the recovery, a behaviour that is not desired for printing. The decrease in SP (D5SP) increased the viscosity in the 12 rpm regime, from 14 to 90 Pa s compared to D3SF. When the rpm decreases to 0.6, a significant recovery in viscosity is measured up to 1900 Pa s. In this case, the viscosity recovery curve of D5SP corresponded with the curve of the benchmark (1950 Pa s). The introduction of microfibers (D6MF) increased the viscosity in the 12 rpm regime to 167 Pa s and shows an instant and significant higher recovery behaviour (4400 Pa s) compared to benchmark and D5SP. Both D5SP and D6MF show a similar recovery behaviour as the benchmark, indicating that these formulations are suitable for extrusion.

The evolution in viscosity of D1FL and D2FA is similar (Fig. 7A) and D2FA has an overall lower viscosity compared to D1FL (supported by the results in Fig. 6). Both samples show a decrease in viscosity with increasing rpm until 10 rpm, indicating shear-thinning due to the breakdown of flocculated particles when shearing [77]. At a shear rate higher than 10 rpm, the viscosity of D1FL and D2FA increases, a behaviour which can be identified as shear-thickening [78]. Shear-thickening is undesired for pumping and can be related to the friction between the particles [79], which can be significant when the proper particle packing is not achieved [80]. The introduction of SF (D3SF) changed the gradient of the viscosity curve, as it exhibited a stronger shear-thinning behaviour compared to D2FA. A stronger shear-thinning behaviour is desired as it benefits buildability, indicated as a high viscosity at a low shear rate (from 87 to 342 Pa s) and pumpability, indicated as low viscosity at a high shear rate (from 20 to 15 Pa s). Further, the shear-thickening behaviour of D3SF is less pronounced compared to D2FA, probably due to the smaller particle size of SF [81]. The increase in viscosity is related to the ultrafine particles of SF which can increase the connectivity between particles and consequently increase the viscosity [82].

Increasing the sand to binder ratio (D4CS) did not change the slope of the viscosity curve but increased the absolute viscosity, implying that the buildability is increased at the expense of the pumpability, which is not desired. Therefore, the sand to binder ratio is kept low, which is in accordance with the desired particle packing. A decrease in SP (D5SP) steepens the viscosity curve (Fig. 7B) with viscosity values at low rpm up to 407 310 Pa s and at high rpm up to 38.5 Pa s, indicating a significant shear-thinning behaviour. The viscosity curve of D6MF overlaps with the curve of D5SP, implying that the introduction of MF did not significantly affect the apparent viscosity. The viscosity values at low rpm of D5SP and D6MF are comparable to the benchmark. However, at high rpm, the viscosity of D5SP and D6MF is higher compared to the benchmark.

The evolution in stress with rotational speed is shown in Fig. 7C and indicates that the stress difference between D1FL and D2FA is small, both showing a stress increase with increasing rotational speed. D2FA exhibited a stress at 100 rpm which is 50% lower compared to D1FL, indicating that the pumpability is improved. The decrease in stress can be related to the spherical particles of FA, which likely decreased the friction between the particles in the mixture compared to the angular NFMS particles. FA might also have contributed to the repulsion effect between particles [82]. The introduction of SF (D3SF) changed the gradient of the stress curve in comparison to D2FA. A higher stress is obtained at low rpm (from 0.9 to 3.4 Pa) due to the increase of inter-particle interactions [83], while at 100 rpm, a lower stress (from 1992 to 1544 Pa) is reached. A yield stress could not be determined for D3SF. Furthermore, increasing the sand to binder ratio resulted in an increase in stress at high shear rates, due to the increase in friction, but did not result in the formation of a yield stress. A yield, however, is required for the buildability.

The absence of yield stress can be related to the amount of SP used in the formulation. If an excess of SP is present in the mixture, the SP is absorbed on all positively-charged surfaces from the OPC particles and hydration phases, preventing flocculation and the formation of yield stress [84,85]. Therefore, the SP is decreased (D5SP), which resulted in a significant increase in stress at low rpm from 3.4 to 2013 Pa (Fig. 7D). A yield stress formed as the number of physical interactions in the fresh

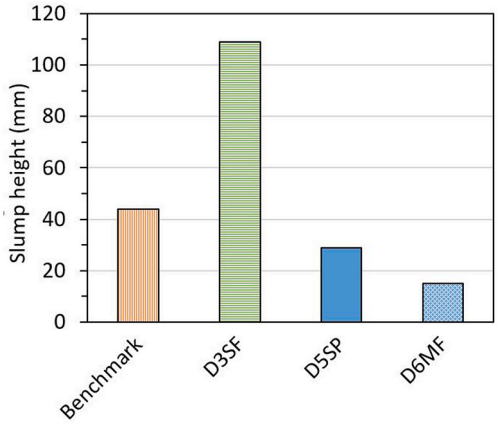

Fig. 8. The individual slump height (in mm) of benchmark, D3SF, D5SP and D6MF 15 min after starting mixing.

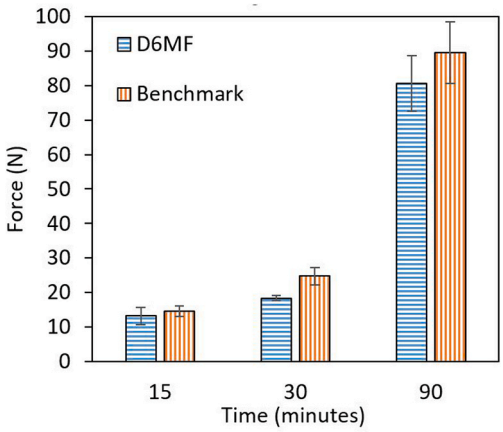

Fig. 9. The average maximum force with error bars that D6MF and benchmark could withstand when applying a vertical compression at 15, 30 and 90 min after starting mixing.

mortar increases, flocs are formed, and less free water is present in the mortar. The yield stress slightly increased from 2013 to 2330 Pa when introducing MF (D6MF). This increase is related to the ultrafine fibres, which increased the surface area and likely resulted in faster flocculation of particles and stronger network connectivity [86]. Both D5SP and D6MF showed similar stress at 100 rpm (2711 Pa), indicating that the fibres did not have a negative effect on the stress at high rpm. This effect might be related to the alignment of the fibres according to the shear direction, increasing the thixotropic effect of the mixture [76]. The yield stress of D5SP and D6MF is similar to the yield stress of the benchmark. The stress at high rpm, however, is higher compared to all other investigated hybrid mixtures and the benchmark.

In general, the benchmark viscosity and stress at high rpm are lower compared to all hybrid mortars, which is likely related to the higher water content in the benchmark and more OPC on which SP can be effective. These two factors probably decreased the friction between particles at high rpm and thus also the stress. Additionally, the SP in hybrid mixtures is likely less effective on the NFMS particles as the NFMS probably has a different surface charge compared to OPC. In this way, there is little steric hindrance between the NFMS particles and the stress at high rpm is increased. D5SP and D6MF are the most promising formulations for 3D printing from a rheological point of view with respect to the pumpability and extrudability despite their relatively high stress at high rpm.

3.3.5. *Slump height, fresh state vertical deformation and setting time*

The slump height of the benchmark, D3SF, D5SP and D6MF is presented in Fig. 8 and shows for the benchmark a height of 44 mm, which can be classified as a 'true slump' [87]. D3SF reached a slump height of 109 mm which can be classified as collapse. This behaviour is typical for self-levelling mixtures which don't have yield stress (Fig. 7C). It is obvious that D3SF would not retain its shape when extruded and therefore it is not suitable for printing. The slump height is decreased to 29 mm when decreasing the SP amount (D5SP) and can be classified as a true slump behaviour. This slump value – combined with the fast recovery in viscosity (Fig. 6) and the presence of yield stress (Fig. 7C) – indicates that the shape can be retained once the mixture is extruded. The introduction of MF (D6MF) resulted in a further decrease in slump height (15 mm), which is closely situated to a zero-slump behaviour. The mixture showed negligible deformation.

The vertical deformation test gives the maximum force of loading at which the structural build-up in the mixture fails and the mixture starts yielding. The structure build-up indicates the strength of the material in fresh state defined by physical interactions and early age reactions, thus prior to hardening. This technique can give insight into the print height or the number of layers (or force) the bottom layer can withstand before yielding. The vertical deformation of D5SP could not be measured as it already collapsed when demoulding the sample, implying that the strength is insufficient. D6MF showed an increase in maximum force with time, of 11.4, 24.8 and 80.5 N, at respectively 15, 30 and 90 min (Fig. 9). The addition of MF contributed to the early-age strength of the material and the evolution of average maximum force of D6MF at 30 and 90 min is similar compared to the benchmark. A two-sample *t*-test was conducted to indicate whether the values for D6MF and the benchmark at 15, 30 and 90 min are different or not. The calculated P-values are 0.592, 0.144 and 0.399 for respectively 15, 30 and 90 min. These P-values are relatively high and indicate that D6MF and the benchmark are statistically not different. A more extended dataset of each sample could lead to lower P-value and potentially to a better indication whether the results are different or not. However, the goal of this research was to obtain properties similar to the benchmark. Therefore, it can be stated that, based on Fig. 9, D6MF follows the same evolution in maximum force as the benchmark.

The setting time is measured for D6MF and the benchmark (shown in Table 6). The initial setting time of D6MF (2.8 h) is 0.8 h earlier compared to the benchmark (3.6 h). The setting time period of D6MF (0.7 h) is more than 4 times shorter than the benchmark (2.9 h). The initial setting time can be related to the open time in which the samples can be printed. The setting period of D6MF and benchmark is initiated

Table 6
The setting time (in hour) of benchmark and M6MF.

Sample	Initial	Final	Period
Benchmark	3.6	6.5	2.9
D6MF	2.8	3.5	0.7

Table 7
Identified mineral phases from Fig. 10, taking into account XRD results of Table 2.

Number	Identified mineral phase
1	Quartz
2	Calcite
3	C_2S
4	Fe-rich slag particle
5	Wüstite
6	Spinel
7	$C_2(A,F)$, C_3A or AFm
8	(K,C)–S–H binder
9	(K,C)-(A,F)–S–H binder
10	(K,C)-A-S-H binder

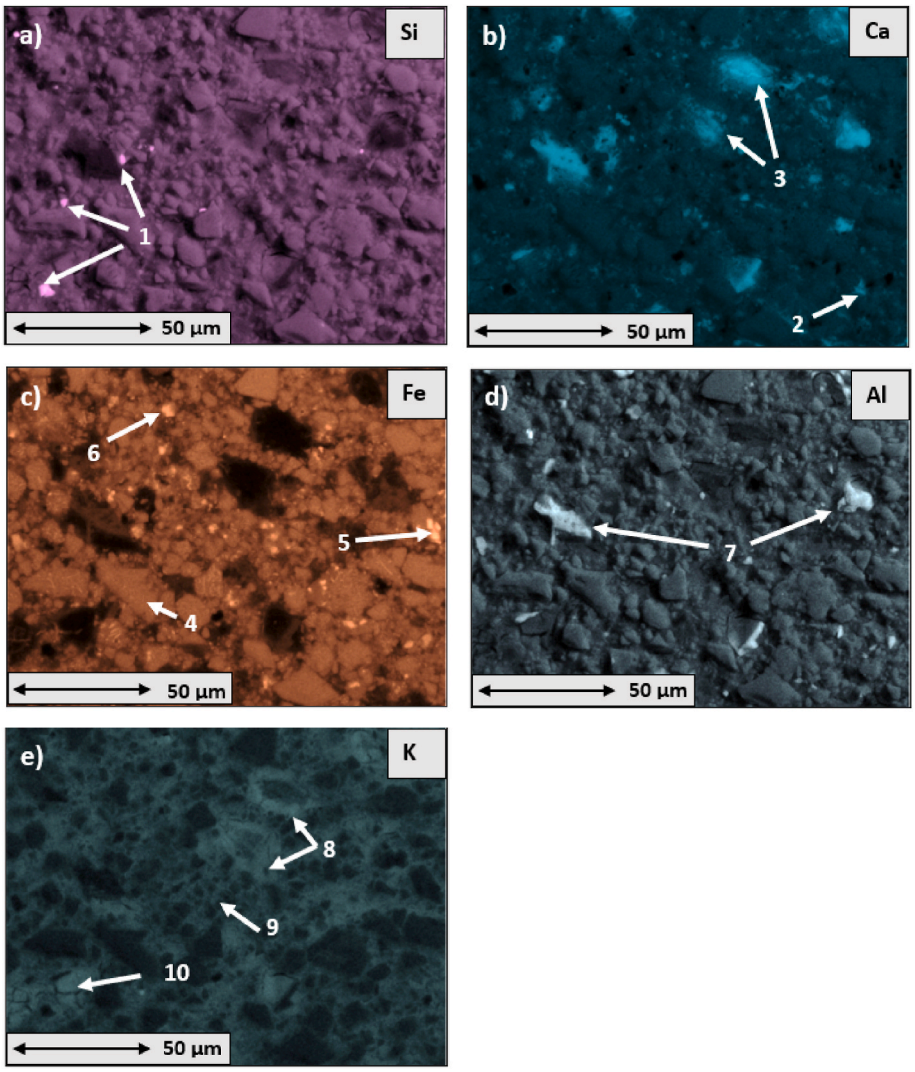

Fig. 10. Polished cross-section of B2SP with elemental mapping of (a) Si, (b) Ca, (c) Fe, (d) Al and (e) K. The numbers are identified in Table 7.

halfway through the 1st acceleration step of their E-mod development (Fig. 5B) and is finished at the end of the 1st step. This acceleration step is likely related to the formation of a physical connected structure, due to flocculation, and the possible early-age precipitation of binder, which took place before the main hydration peak. This implies that the samples at the final setting time are hardened but their main strength development (at the main hydration peak) did not take place yet.

3.3.6. *Microstructural analysis*

Elemental mapping of Si, Ca, Fe, Al, and K is performed on the microstructure of B2SP. Formulation B2SP consists of only OPC, NFMS and SP, and thus enables easier identification of the different phases. The identification would be more challenging in a hybrid made from several raw materials (such as D6MF). Fig. 10A shows that some small spots are only enriched in Si (1 in Fig. 10A), which can be identified as quartz, as expected from the XRD results (Table 2). Fig. 10C shows various zones enriched in Ca and poor in Si (2 in Fig. 10B), which can be identified as calcite due to carbonation. Other areas, which look like particles, are dominant in only Ca and Si (3 in Fig. 10B), and can be identified as relicts from OPC, such as C_2S, implying that no full hydration took place. The Fe distribution in Fig. 10C shows that most grains (4 in Fig. 10C) are rich in Fe. These grains can be considered NFMS. In the NFMS particles, Fe-rich and Ca- and Si-poor zones (5 in Fig. 10C) are identified, which can be assigned to wüstite. Some Fe-rich zones are also rich in Al (6 in Fig. 10D) and are found as separate grains or as a part of the NFMS. These zones are identified as spinels. Fig. 10D shows two grains, rich in Ca and Al, and a minor amount of Fe (7 in Fig. 10D), which can be identified as ferrite, AFm or C_3A phases from OPC.

The K is distributed between the particles and originated from the activating solution. In all probability, the K is incorporated in the binder and thus the K-rich zones can be considered predominantly as binder. A Si, Ca and K-rich zone (8 in Fig. 10E) is identified around the C_3S phase, suggesting that the C_3S is partially dissolved and that a (K,C)–S–H binder is formed around the C_3S. The binder between the small NFMS particles, situated in the centre of Fig. 10E is dominant in K, Si and Fe (9 in Fig. 10E), suggesting a (K,C)-(A,F)–S–H binder due to the contribution of Fe and Al from the NFMS. Another zone is identified which is low in Fe and Ca (10 in Fig. 10E), suggesting the presence of a (K,C)-A-S-H binder.

Based on the phases identified in Fig. 10 and the data from the chemical point analysis of D6MF (not shown here for the sake of brevity) it is clear that the binder chemistry is not similar throughout the matrix. Some binder zones are enriched in Fe, Al or Ca, depending on whether they are situated close to an NFMS particle (influx of Fe and Al), FA (influx of Al) or OPC (Ca and/or Al enriched) and a transition from one zone to the other is identified. The Al is likely incorporated into the initially formed C–S–H binder [70] to form a (K,C)-A-S-H, while the Fe probably partially replaced Al [88] to form a (K,C)-(A,F)–S–H binder. The presence of Fe in the binder shows that the NFMS dissolved,

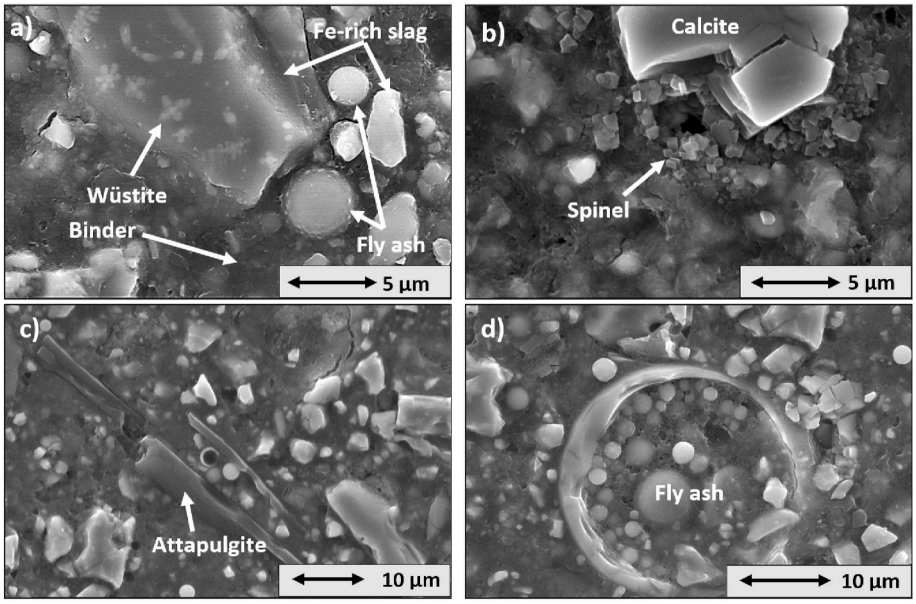

Fig. 11. (a) and (b): the microstructure of D6MF taken with SEM at magnification 5000. Panel (c) SEM image at magnification 2000 and (d) at magnification 2500.

contributed to the binder and thus can be considered as a precursor.

The microstructure of D6MF is shown in Fig. 11 and wüstite minerals can be identified in the NFMS (Fig. 11A), next to calcite particles from the FL and spinel from the NFMS (Fig. 11B). MF or attapulgite minerals of around 20 µm in length were also identified in the matrix (Fig. 11C) and seem not reacted. Next to the NFMS particles, FA is situated throughout the matrix and consisted of different sizes (Fig. 11A and D).

4. Conclusion

A hybrid mortar formulation for 3D printing is developed in which the amount of OPC is kept to a minimum and NFMS is used as the main precursor. The developed hybrid mortar needs to comply with the print criteria, i.e. shear-thinning, high yield stress, and early-age stiffness development. These criteria were identified by an OPC-based 3D-printable mixture used as benchmark. Several raw materials, such as FA, SF, FL and CS are introduced in the hybrid mortar with specific proportions. The main findings of this research are mentioned below.

- The introduction of FA in the hybrid mortar improved the pumpability and accelerated the reactivity.
- The addition of SF and the decrease in SP improved the shear-thinning behaviour, led to the formation of yield stress and accelerated the reactivity of a hybrid mortar. With these changes in mix design (D5SP) the evolution in dynamic E-modulus was accelerated and exceeded the one of the benchmark.
- The introduction of MF did not affect the reactivity and the final developed formulation (D6MF) showed a cement hydration peak at 12 h, followed by a slag reaction peak at 27 h. MF in the hybrid mortar increased the yield stress without significantly affecting the pumpability and improved the early-age strength build-up and slump height in such a way that it reached the criteria.
- The proportion of CS, SP and MF are chosen in such a way that the rheological requirements are reached. The best developed hybrid mortar for printing is D6MF and its binder is comprised of OPC (13.8 wt%), NFMS (55.9 wt%), FL (7.4 wt%), FA (14.4 wt%), SF (7.4 wt%), SP (0.3 wt%), BA (0.3 wt%), MF (0.2 wt%) and a 1 M KOH with an activator to binder ratio of 0.2. The sand to binder ratio is 1.
- Three acceleration steps in dynamic E-modulus development were identified in the hybrid mortar, of which the first one is related to the build-up of a physically connected structure, the second is related to the main hydration and its associated binder formation, and the third step is related to the NFMS contribution.
- Elemental mapping showed that Fe is situated in the binder. In that case, it can be concluded that the NFMS is not inert, but dissolved and contributed to the binder formation.

This research shows that the NFMS contributes to the binder formation and strength development and thus can be considered a precursor. Based on the results in this study it is possible to develop a mortar with a low amount of OPC, with fresh state print characteristics similar to an OPC-based 3D-printable mortar. The development of the 3D-printable hybrid mortar from NFMS can increase the valorisation potential of these slags for construction applications.

Declaration of competing interest

The authors declare the following financial interests/personal relationships which may be considered as potential competing interests: Glenn Beersaerts reports financial support was provided by Center for Resource Recovery and Recycling.

Data availability

Data will be made available on request.

Acknowledgements

The authors would like to thank Prof. Theo Salet and Dr. Rob Wolfs from the University of Technology Eindhoven for the interesting discussions and their hospitality to use the lab facilities of the university. The authors would also like to thank M. Suijs and B. Rijssen for their assistance during the experiments. The authors would like to acknowledge the Center for Resource, Recovery and Recycling (CR3) and the partners therein for funding this research (https://wp.wpi.edu/cr3/). The authors declare that there is no conflict of interest regarding the publication of this article.

References

[1] R.d. Laubier, M. Wunder, S. Witthöft, C. Rothballer, Will 3D Printing Remodel the Construction Industry? The Boston Consulting Group, 2018.
[2] M.v. Sante, ConTech: Technologie in de bouw, 2018.

[3] F. Barbosa, J. Woetzel, J. Mischke, M.J. Ribeirinho, M. Sridhar, M. Parsons, N. Bertram, S. Brown, Reinventing Construction: a Route to Higher Productivity, McKinsey Global Institute, 2017.

[4] I. Kothman, N. Faber, How 3D printing technology changes the rules of the game, J. Manuf. Technol. Manag. 27 (2016) 932–943.

[5] Y.W.D. Tay, B. Panda, S.C. Paul, N.A. Noor Mohamed, M.J. Tan, K.F. Leong, 3D printing trends in building and construction industry: a review, Virtual Phys. Prototyp. 12 (2017) 261–276.

[6] Y. Chen, O. Copuroglu, F. Veer, A critical review of 3D concrete printing as a low CO2 concrete approach, Heron 62 (2017).

[7] N. Khalil, G. Aouad, K. El Cheikh, S. Rémond, Use of calcium sulfoaluminate cements for setting control of 3D-printing mortars, Construct. Build. Mater. 157 (2017) 382–391.

[8] N. Khalil, S. Rémond, B. Baz, G. Aouad, Characterization of 3D printing mortars made with OPC/CSA mixes, in: T. Wangler, R.J. Flatt (Eds.), First RILEM International Conference on Concrete and Digital Fabrication: Digital Concrete 2018, Springer International Publishing, 2018, pp. 53–60.

[9] P. Chaunsali, P. Mondal, Physico-chemical interaction between mineral admixtures and OPC–calcium sulfoaluminate (CSA) cements and its influence on early-age expansion, Cement Concr. Res. 80 (2016) 10–20.

[10] T.T. Le, S.A. Austin, S. Lim, R.A. Buswell, A.G.F. Gibb, T. Thorpe, Mix design and fresh properties for high-performance printing concrete, Mater. Struct. 45 (2012) 1221–1232.

[11] C. Li, X.Z. Gong, S.P. Cui, Z.H. Wang, Y. Zheng, B.C. Chi, CO2 emissions due to cement manufacture, MSF 685 (2011) 181–187.

[12] C.A. Hendriks, E. Worrell, L. Price, N. Martin, L. Ozawa Meida, D. de Jager, P. Riemer, Emission reduction of greenhouse gases from the cement industry, Mater. Sci. (2003) 939–944.

[13] G. de Schutter, K. Lesage, V. Mechtcherine, V.N. Nerella, G. Habert, I. Agusti-Juan, Vision of 3D printing with concrete — Technical, economic and environmental potentials, Cement Concr. Res. 112 (2018) 25–36.

[14] Y. Chen, S. He, Y. Zhang, Z. Wan, O. Çopuroğlu, E. Schlangen, 3D printing of calcined clay-limestone-based cementitious materials, Cement Concr. Res. 149 (2021), 106553.

[15] Y. Chen, C. Romero Rodriguez, Z. Li, B. Chen, O. Çopuroğlu, E. Schlangen, Effect of different grade levels of calcined clays on fresh and hardened properties of ternary-blended cementitious materials for 3D printing, Cement Concr. Compos. 114 (2020), 103708.

[16] H. Alghamdi, S.A. Nair, N. Neithalath, Insights into material design, extrusion rheology, and properties of 3D-printable alkali-activated fly ash-based binders, Mater. Des. 167 (2019), 107634.

[17] S.C. Paul, Y.W.D. Tay, B. Panda, M.J. Tan, Fresh and hardened properties of 3D printable cementitious materials for building and construction, Arch. Civ. Mech. Eng. 18 (2018) 311–319.

[18] B. Panda, S.C. Paul, N.A.N. Mohamed, Y.W.D. Tay, M.J. Tan, Measurement of tensile bond strength of 3D printed geopolymer mortar, Measurement 113 (2018) 108–116.

[19] B. Panda, M.A.N. Nisar, T.J. Ming, Effect of 3D printing on mechanical properties of fly ash-based inorganic geopolymer, in: M.M. Reda Taha (Ed.), International Congress on Polymers in Concrete: Polymers for Resilient and Sustainable Concrete Infrastructure, Springer International Publishing, 2018, pp. 509–515.

[20] A. Kashani, T. Ngo, Optimisation of Mixture Properties for 3D Printing of Geopolymer Concrete, 35th International Symposium on Automation and Robotics in Construction, 2018.

[21] A. Albar, M. Chougan, M.J. al- Kheetan, M.R. Swash, S.H. Ghaffar, Effective extrusion-based 3D printing system design for cementitious-based materials, Results Eng. 6 (2020), 100135.

[22] European Commission, Communication from the Commission: the European Green Deal, 2019. https://eur-lex.europa.eu/legal-content/EN/TXT/?uri=COM%3A2019%3A640%3AFIN.

[23] R. Snellings, Assessing, understanding and unlocking supplementary cementitious materials, RILEM Tech. Lett. 1 (2016) 50.

[24] J.L. Provis, J.S.J. Van Deventer, Geopolymers and other alkali-activated materials, in: P. Hewlett, M. Liska (Eds.), Lea's Chemistry of Cement and Concrete, fifth ed., Butterworth-Heinemann, 2019, pp. 779–805.

[25] A. Peys, Inorganic Polymers from CaO-FeO-SiO2 Slags: Processing, Reaction Mechanism and Molecular Structure, Dissertation, KU Leuven Belgium, 2018.

[26] L. Kriskova, L. Machiels, Y. Pontikes, Inorganic polymers from a plasma convertor slag: effect of activating solution on microstructure and properties, Journal of Sustainable Metallurgy 1 (2015) 240–251.

[27] A. Peys, L. Arnout, B. Blanpain, H. Rahier, K. Van Acker, Y. Pontikes, Mix-design parameters and real-life considerations in the pursuit of lower environmental impact inorganic polymers, Waste and Biomass Valorisation 9 (2018) 879–889.

[28] L.K. Turner, F.G. Collins, Carbon dioxide equivalent (CO2-e) emissions: a comparison between geopolymer and OPC cement concrete, Construct. Build. Mater. 43 (2013) 125–130.

[29] M. Palacios, Y.F. Houst, P. Bowen, F. Puertas, Adsorption of superplasticizer admixtures on alkali-activated slag pastes, Cement Concr. Res. 39 (2009) 670–677.

[30] A. Fernández-Jiménez, I. García-Lodeiro, S. Donatello, O. Maltseva, Á. Palomo, Specific examples of hybrid alkaline cement, MATEC Web Conference 11 (2014) 1001.

[31] I. Garcia-Lodeiro, O. Maltseva, A. Palomo, A. Fernandez-Jiménez, Hybrid alkaline cements. Part I: fundamentals, Romanian, J. Mater. 42 (2012) 330–335.

[32] A. Palomo, A. Fernández-Jiménez, G. Kovalchuk, L.M. Ordoñez, M.C. Naranjo, Opc-fly ash cementitious systems: study of gel binders produced during alkaline hydration, J. Mater. Sci. 42 (2007) 2958–2966.

[33] S. Alonso, Á. Palomo, Alkaline activation of metakaolin and calcium hydroxide mixtures: influence of temperature, activator concentration and solids ratio, Mater. Lett. 47 (2001) 55–62.

[34] I. Garcia-Lodeiro, A. Palomo, A. Fernández-Jiménez, D.E. Macphee, Compatibility studies between N-A-S-H and C-A-S-H gels. Study in the ternary diagram Na2O–CaO–Al2O3–SiO2–H2O, Cement Concr. Res. 41 (2011) 923–931.

[35] L. Arnout, G. Beersaerts, M. Liard, D. Lootens, Y. Pontikes, Valorising slags from non-ferrous metallurgy into hybrid cementitious binders: mix design and performance, Waste and Biomass Valorisation 12 (2021) 4679–4694.

[36] J. Plank, C. Hirsch, Impact of zeta potential of early cement hydration phases on superplasticizer adsorption, Cement Concr. Res. 37 (2007) 537–542.

[37] D. Ectors, J. Neubauer, F. Goetz-Neunhoeffer, The hydration of synthetic brownmillerite in presence of low Ca-sulfate content and calcite monitored by quantitative in-situ-XRD and heat flow calorimetry, Cement Concr. Res. 54 (2013) 61–68.

[38] L. Arnout, Y. Pontikes, Fe-rich Binder, 2019. WO/2020/025691.

[39] T. Hertel, Binders and Monoliths from Bauxite Residue (Red Mud), 2020. Dissertation, KU Leuven Belgium.

[40] G. Ma, Z. Li, L. Wang, Printable properties of cementitious material containing copper tailings for extrusion based 3D printing, Construct. Build. Mater. 162 (2018) 613–627.

[41] G. Beersaerts, S.S. Lucas, Y. Pontikes, An Fe-Rich Slag-Based Mortar for 3D Printing 28 3–12.

[42] B. Panda, G.B. Singh, C. Unluer, M.J. Tan, Synthesis and characterization of one-part geopolymers for extrusion based 3D concrete printing, J. Clean. Prod. 220 (2019) 610–619.

[43] B. Panda, C. Unluer, M.J. Tan, Investigation of the rheology and strength of geopolymer mixtures for extrusion-based 3D printing, Cement Concr. Compos. 94 (2018) 307–314.

[44] G.M.S. Islam, M.T. Raihan, M.M. Hasan, M. Rashadin, Effect of retarding superplasticizers on the properties of cement paste, mortar and concrete, Asian J. Civil Eng. 20 (2019) 591–601.

[45] F. Puertas, A. Palomo, A. Fernandez-Jimenez, J.D. Izquierdo, M.L. Granizo, Effect of superplasticisers on the behaviour and properties of alkaline cements, Adv. Cement Res. 15 (2003) 23–28.

[46] F. Bos, R. Wolfs, Z. Ahmed, T. Salet, Additive manufacturing of concrete in construction: potentials and challenges of 3D concrete printing, Virtual Phys. Prototyp. 11 (2016) 209–225.

[47] N. Roussel, Rheological requirements for printable concretes, Cement Concr. Res. 112 (2018) 76–85.

[48] L.N. Thrane, C. Pade, C.V. Nielsen, A.A. Jeknavorian, J.J. Schemmel, S.W. Dean, Determination of rheology of self-consolidating concrete using the 4C-rheometer and how to make use of the results, J. ASTM Int. (JAI) 7 (2010), 102003.

[49] B. Nematollahi, M. Xia, J. Sanjayan, P. Vijay, Effect of type of fiber on inter-layer bond and flexural strengths of extrusion-based 3D printed geopolymer, Mater. Sci. Forum 939 (2018) 155–162.

[50] K. Korniejenko, M. Łach, Geopolymers reinforced by short and long fibres – innovative materials for additive manufacturing, Curr. Opin. Chem. Eng. 28 (2020) 167–172.

[51] R. Snelling, L. Machiels, G. Mertens, J. Elsen, Rietveld refinement strategy for quantitative phase analysis of partially amorphous zeolitized tuffaceous rocks, Geol. Belg. 13 (2010) 183–196.

[52] S. Fennis, J. Walraven, Using particle packing technology for sustainable concrete mixture design, Heron 57 (2012) 73–101.

[53] S. Kumar, M. Santhanam, Particle Packing Theories and Their Application in Concrete Mixture Proportioning: A Review, The Indian Concrete Journal, 2003.

[54] EN 12504-4 2004, Testing Concrete - Part 4: Determination of Ultrasonic Pulse Velocity, 30, European Committee for Standardization, Brussels, Belgium 91, 2004, 100.

[55] C09 Committee, Test Method for Slump of Hydraulic-Cement Concrete, ASTM International, West Conshohocken, PA, 2016.

[56] R. Wolfs, F.P. Bos, T. Salet, Early age mechanical behaviour of 3D printed concrete: numerical modelling and experimental testing, Cement Concr. Res. 106 (2018) 103–116.

[57] ASTM D2166, Standard Test Method for Unconfined Compressive Strength of Cohesive Soil, ASTM International, West Conshohocken, 2016. PA 93.020.

[58] EN 196-3:2017, Methods for testing cement: Part 3: determination of setting times and soundness, Eur. Committee Standardiz. 91 (2016) 100, 10.

[59] A.V. Rahul, M. Santhanam, H. Meena, Z. Ghani, 3D printable concrete: mixture design and test methods, Cement Concr. Compos. 97 (2019) 13–23.

[60] J. Ma, M. Orgass, N. Viet Tue, Influence of addition method of suplerplasticizer on the properties of fresh UHPC, in: E. Fehling, M. Schmidt, S. Stürwald (Eds.), Proceedings of the Second International Symposium on Ultra High Performance Concrete, Kassel, Germany, 2008, pp. 93–100.

[61] B. Graybeal, Characterization of the Behavior of Ultra-high Performance Concrete, University of Maryland, 2005.

[62] H.F.W. Taylor, Cement Chemistry, second ed., Thomas Telford, London, 1997.

[63] D.P. Bentz, Influence of water-to-cement ratio on hydration kinetics: simple models based on spatial considerations, Cement Concr. Res. 36 (2006) 238–244.

[64] K. Yoshioka, E. Tazawa, K. Kawai, T. Enohata, Adsorption characteristics of superplasticizers on cement component minerals, Cement Concr. Res. 32 (2002) 1507–1513.

[65] F. Kreppelt, M. Weibel, D. Zampini, M. Romer, Influence of solution chemistry on the hydration of polished clinker surfaces—a study of different types of polycarboxylic acid-based admixtures, Cement Concr. Res. 32 (2002) 187–198.

[66] N. Robeyst, N. De Belie, Effect of superplasticizers on hydration and setting behaviour of cements, in: P. Gupta, T. Holland, V. Malhotra (Eds.), Ninth ACI International Conference on Superplasticizers and Other Chemical Admixtures in Concrete, American Concrete Institute, 2009, pp. 61–73.
[67] D. Torréns-Martín, L. Fernández-Carrasco, Effect of sulfate content on cement mixtures, Construct. Build. Mater. 48 (2013) 144–150.
[68] L. Xu, P. Wang, G. Zhang, Calorimetric study on the influence of calcium sulfate on the hydration of Portland cement–calcium aluminate cement mixtures, J. Therm. Anal. Calorim. 110 (2012) 725–731.
[69] K.L. Scrivener, P. Juilland, P.J. Monteiro, Advances in understanding hydration of Portland cement, Cement Concr. Res. 78 (2015) 38–56.
[70] I. García-Lodeiro, A. Fernández-Jiménez, A. Palomo, Variation in hybrid cements over time. Alkaline activation of fly ash–portland cement blends, Cement Concr. Res. 52 (2013) 112–122.
[71] I.F. Saez del Bosque, S. Martinez-Ramirez, M.T. Blanco-Varela, Calorimetric study of white portland cement hydration. Effect of nanosilica and temperature, in: C. Shi, Y. Yao (Eds.), ICCC 2015 Beijing: the 14th International Congress on the Chemistry of Cement, Chinese Ceramic Society, 2015.
[72] R. Siddique, M.I. Khan, Supplementary Cementing Materials, Springer Berlin Heidelberg, Berlin, Heidelberg, 2011.
[73] M.-H. Zhang, K. Sisomphon, T.S. Ng, D.J. Sun, Effect of superplasticizers on workability retention and initial setting time of cement pastes, Construct. Build. Mater. 24 (2010) 1700–1707.
[74] D.P. Bentz, T. Sato, I. de La Varga, W.J. Weiss, Fine limestone additions to regulate setting in high volume fly ash mixtures, Cement Concr. Compos. 34 (2012) 11–17.
[75] S. Bauchkar, H. Chore, Effect of PCE superplasticizers on rheological and strength properties of high strength self-consolidating concrete, Adv. Concrete Construct. 6 (2018) 561–583.
[76] Z. Quanji, Thixotropic Behavior of Cement-Based Materials: Effect of Clay and Cement Types, Iowa State University, Dissertation, 2010.
[77] L. Struble, G.-K. Sun, Viscosity of Portland cement paste as a function of concentration, Adv. Cement Base Mater. 2 (1995) 62–69.
[78] D. Feys, R. Verhoeven, G. de Schutter, Fresh self compacting concrete, a shear thickening material, Cement Concr. Res. 38 (2008) 920–929.
[79] Z. Pan, H. de Cagny, B. Weber, D. Bonn, S-shaped flow curves of shear thickening suspensions: direct observation of frictional rheology, Phys. Rev. E: Stat., Nonlinear, Soft Matter Phys. 92 (2015).
[80] W. Cai, Effect of Particle Packing on Flow Property and Strength of Concrete Mortar, Iowa State University, Dissertation, 2017.
[81] D. Feys, R. Verhoeven, G. de Schutter, Why is fresh self-compacting concrete shear thickening? Cement Concr. Res. 39 (2009) 510–523.
[82] J.A. Correa-Yepes, N. Rojas-Reyes, I.T. Jorge, Effect of fly ash and silica fume on rheology, compressive strength and self-compacting in cement mixtures, DYNA 206 (2018) 59–68.
[83] M.O. Bustamante Rúa, N.R. Rojas Reyes, G.R. Quitian Chila, Fine material effect on kaolin suspensions rheology, DYNA 83 (2016) 105–111.
[84] X. Kong, Y. Zhang, S. Hou, Study on the rheological properties of Portland cement pastes with polycarboxylate superplasticizers, Rheol. Acta 52 (2013) 707–718.
[85] J. Björnström, S. Chandra, Effect of superplasticizers on the rheological properties of cements, Mater. Struct. 36 (2003) 685–692.
[86] I. Dejaeghere, M. Sonebi, G. de Schutter, Influence of nano-clay on rheology, fresh properties, heat of hydration and strength of cement-based mortars, Construct. Build. Mater. 222 (2019) 73–85.
[87] EN 12350-2:2019, Testing Fresh Concrete: Part 2: Slump Test, European Committee for Standardization 91.100.30, 2019.
[88] A. Peys, A.P. Douvalis, V. Hallet, H. Rahier, B. Blanpain, Y. Pontikes, Inorganic polymers from CaO-FeOx-SiO2 slag: the start of oxidation of Fe and the formation of a mixed valence binder, Front. Mater. 6 (2019).